Measurement of the Self-Sensing Capability of Synchronous Machines for High Frequency Signal Injection Sensorless Drives

Matteo Berto, Luigi Alberti, *Senior Member, IEEE*, and Silverio Bolognani, *Fellow, IEEE*

***Abstract*—Signal injection sensor-less control for synchronous machines is known to be afflicted by an estimation error dependent on the load current. The estimation error is related to the cross-saturarion and the saliency of the adopted synchronous machine. A motor can be more or less suitable for signal injection sensorless control compared to other motors with different designs or sizes. A sensorless drive can even be afflicted by the control divergence when the machine is highly saturated, resulting in a useless drive. Moreover, even when the control converges, the actual current control trajectory is different from the given reference. In this paper, a measurement procedure of the convergence region, i.e. the operating points where the motor can be successfully controlled without a position sensor is presented and validated. In particular, two different synchronous motors are considered, a permanent magnet assisted synchronous reluctance motor (PMA-SynRM) and a synchronous reluctance motor (SynRM).**

***Index Terms*—Finite element analysis, inductance, modeling, motor drives, permanent magnet motors, sensorless control.**

NOMENCLATURE

$\alpha\beta$	Stator reference frame.
dq	Rotor reference frame.
$d^x q^x$	Estimated rotor reference frame.
θ_{me}	Rotor electrical position (rad)
$\tilde{\theta}_{me}$	Estimated rotor electrical position (rad)
ε	Estimation error in open loop (rad)
I_{hq}	Input of the position observer (A)
hf	High-frequency.
U_h	Amplitude of the voltage injection (V)
f_h	Frequency of the voltage injection (Hz)
MTPA	Maximum torque per ampere.
REF	Reference for the current control loop.
t_1	Sensored (fictitious) current trajectory.
t_2	Sensorless current trajectory.
PMA-SynRM	Permanent magnet assisted synchronous reluctance motor.
SynRM	Synchronous reluctance motor.

Manuscript received 30 June 2022; revised 7 October 2022 and 12 January 2023; accepted 29 January 2023. Date of publication 3 February 2023; date of current version 19 May 2023. Paper 2022-IDC-0821.R2, presented at the 2021 IEEE Energy Conversion Congress and Exposition, Vancouver, BC Canada, Oct. 10–14, and approved for publication in the IEEE TRANSACTIONS ON INDUSTRY APPLICATIONS by the Industrial Drives Committee of the IEEE Industry Applications Society [DOI: 10.1109/ECCE47101.2021.9595287]. *(Corresponding author: Luigi Alberti.)*

The authors are with the Dept. of Industrial Engineering, University of Padova, 35131 Padova, Italy (e-mail: matteo.berto@studenti.unipd.it; luigi.alberti@unipd.it; silverio.bolognani@unipd.it).

Color versions of one or more figures in this article are available at https://doi.org/10.1109/TIA.2023.3241887.

Digital Object Identifier 10.1109/TIA.2023.3241887

I. INTRODUCTION

POSITION sensors such as encoders and resolvers are conventionally required to control synchronous reluctance motors (SynRM) and permanent magnet assisted synchronous reluctance motors (PMA-SynRM). In the last thirty years, the control of synchronous motors removing the position sensor has been investigated and properly achieved. Many valid sensorless techniques exist, depending on the operational conditions of the motor. At high speed, the sensorless control usually adopt observers or estimators in order to reconstruct the machine state and hence the rotor position [1], [2], [3]. In the zero-low speed region (usually up to a tenth of the rated speed), additional signal injection are used to identify the rotor position. [4], [5]. Different approaches have been proposed in literature exploiting high frequency carrier signal and demodulation [6], [7] or unconventional pulse-width modulation (PWM) patterns [8], [9].

Signal injection sensorless control is known to be affected by the variation of the motor differential inductances with the operating point [10]. In particular, it appears that some motors can be more suitable than others to be controlled without a position sensor.

The convergence region [11], [12] should be computed to know if a motor is suitable for signal injection sensorless control. The flux linkages maps, obtainable by finite element analysis (FEA) or experimental measurements (motor characterization), are usually required to compute the convergence region of a sensorless drive [13].

In [14], an experimental procedure to measure the self-sensing capability of a synchronous sensorless drive was introduced. The paper describes a test methodology to measure the sensorless control trajectories introduced in [13]. In particular two different tests are proposed. The first one allows to obtain the sensored trajectory t_1, i.e. the trajectory of the position observer in open-loop during a sensored operation. The second allows to measure the sensorless trajectory t_2 of the drive, i.e. the trajectory of the effective operating points controlling the motor in sensorless operation. In [14] the analysis was limited to considering a PMA-SynRM drive and the trajectory measurement was implemented considering only rotating high frequency (hf) signal

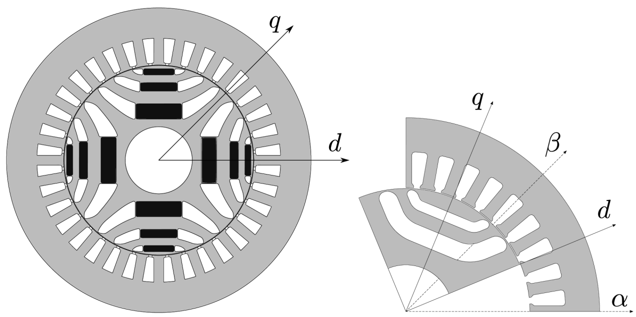

(a) PMA-SynRM geometry (b) SynRM geometry

Fig. 1. Geometries of the considered motors.

TABLE I
MAIN DATA OF THE CONSIDERED MOTORS

	PMA-SynRM	SynRM	
rated peak current	6	3	A
rated torque	16	5.5	Nm
d-axis apparent inductance	0.054	0.45	H
q-axis apparent inductance	0.4	0.1	H
stator resistance	4.6	14	Ω
PM remanence	0.5	–	T

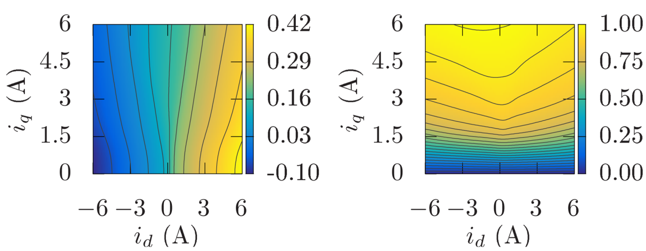

(a) $\lambda_d(i_d, i_q)$ (Vs) (b) $\lambda_q(i_d, i_q)$ (Vs)

Fig. 2. PMA-SynRM flux linkages (finite element analysis) for $\theta_{me} = 0$.

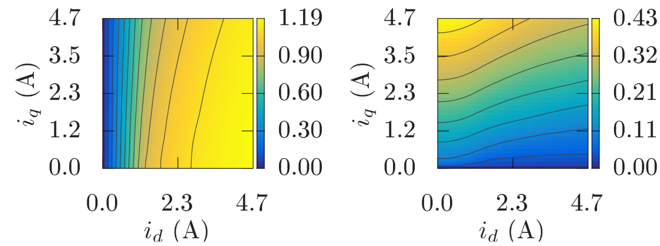

(a) $\lambda_d(i_d, i_q)$ (Vs) (b) $\lambda_q(i_d, i_q)$ (Vs)

Fig. 3. SynRM flux linkages (finite element analysis) for $\theta_{me} = 0$.

injection. This paper extends such an analysis. In particular a second drive of different type, i.e. adopting a SynRM motor, is considered. Moreover, the effect of the injection strategy on the trajectories measurements is investigated. In particular besides rotating injection also pulsating injection is included in this paper. Last, also the effects of different demodulation techniques are investigated in the following. The proposed experimental procedure is compared and validated with computations based on finite element analysis (FEA) results [15].

II. Description of the Considered Motors and Drives

In this paper two different synchronous motors are considered. They are characterized by a significant reluctance torque component and one has been also equipped with PM assistance to improve its performance. The geometries and the conventions adopted to define the rotor reference frame are shown in Fig. 1. Table I summarizes the main data of the considered machines. The motors have been characterized for rotor position $\theta_{me} = 0$ through finite element analysis (FEA). The corresponding flux linkages λ_d and λ_q are shown in Fig. 2 for the PMA-SynRM. Fig. 3 shows the characteristics for the SynRM.

The high-frequency (hf) model of a synchronous motor can be obtained from the voltage equations neglecting the stator resistance and the permanent magnet flux [16]. This assumption is valid because the frequency of the additional signal injection is sufficiently high (usually higher than 500 Hz) [4], [5]. Thus, the hf model of a synchronous motor at quasi-zero speed is:

$$\begin{bmatrix} u_{hd}(t) \\ u_{hq}(t) \end{bmatrix} = \begin{bmatrix} l_{dd} & l_{dq} \\ l_{dq} & l_{qq} \end{bmatrix} \begin{bmatrix} \frac{\partial i_{hd}(t)}{\partial t} \\ \frac{\partial i_{hq}(t)}{\partial t} \end{bmatrix} \tag{1}$$

where u_{hd} and u_{hq} are the injected hf voltages and i_{hd} and i_{hq} the hf currents. The incremental inductances are defined as:

$$l_{dd} = \frac{\partial \lambda_d}{\partial i_d} \qquad l_{qq} = \frac{\partial \lambda_q}{\partial i_q} \tag{2a}$$

$$l_{dq} = \frac{\partial \lambda_d}{\partial i_q} = \frac{\partial \lambda_q}{\partial i_d} \tag{2b}$$

$$l_\Sigma = \frac{l_{qq} + l_{dd}}{2} \qquad l_\Delta = \frac{l_{qq} - l_{dd}}{2} \tag{2c}$$

where l_{dd} is the d-axis incremental inductance, l_{dq} the mutual incremental inductance (also known as cross-saturation inductance), l_{qq} the q-axis incremental inductance, l_Σ the mean incremental inductance and l_Δ the semi-difference incremental inductance.

The incremental inductances are the key parameters in signal injection sensorless control and different injection techniques can be adopted to estimate the rotor position. In the paper, two different injection techniques are adopted. In particular, both pulsating and rotating injections are considered. Moreover, with the rotating injection method, two different position estimation techniques are adopted. The details are described in the following.

A. Sinusoidal Injection in $d^x q^x$ (pulsating)

As shown in Fig. 4, a pulsating hf injection is superimposed to the $d^x q^x$ voltage references:

$$\begin{aligned} u^x_{hd} &= U_h \cos(\omega_h t) \\ u^x_{hq} &= 0 \end{aligned} \tag{3}$$

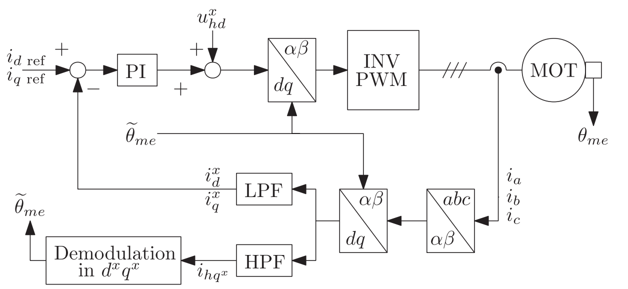

Fig. 4. Control scheme for anisotropic synchronous machines drives: pulsating injection in $d^x q^x$ and demodulation.

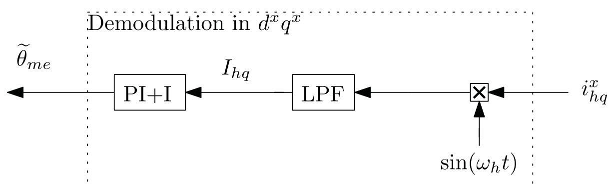

Fig. 5. Demodulation scheme in $d^x q^x$.

The sinusoidal pulsating injection in d^x leads to the high frequency currents:

$$
\begin{aligned}
i_{hd}^x &= I_h \left[l_\Sigma + l_\Delta \cos(2\Delta\theta) - l_{dq} \sin(2\Delta\theta) \right] \sin(\omega_h t) \\
i_{hq}^x &= -I_h \left[l_\Delta \sin(2\Delta\theta) + l_{dq} \cos(2\Delta\theta) \right] \sin(\omega_h t)
\end{aligned} \tag{4}
$$

or, equivalently:

$$
\begin{aligned}
i_{hd}^x &= I_h \left[l_\Sigma + \sqrt{l_\Delta^2 + l_{dq}^2} \cos(2\Delta\theta - 2\varepsilon) \right] \sin(\omega_h t) \\
i_{hq}^x &= -I_h \left[\sqrt{l_\Delta^2 + l_{dq}^2} \sin(2\Delta\theta - 2\varepsilon) \right] \sin(\omega_h t)
\end{aligned} \tag{5}
$$

where:

$$
\begin{aligned}
I_h &= \frac{U_h}{\omega_h \left(l_{dd}\, l_{qq} - l_{dq}^2 \right)} \\
\Delta\theta &= \tilde{\theta}_{me} - \theta_{me}
\end{aligned} \tag{6}
$$

and ε is the estimation error. The hf currents i_{hd}^x, i_{hq}^x are obtained measuring the $d^x q^x$ currents and applying a high-pass filter (HPF). The rotor position information is extracted by a demodulation-observer scheme applied to the current i_{hq}^x, as shown in Fig. 5. The current i_{hq}^x is multiplied for $\sin(\omega_h t)$ and the result is filtered with a low-pass filter (LPF). The result of the demodulation is the signal:

$$
I_{hq} = -\frac{I_h}{2} \left[-l_\Delta \sin(2\Delta\theta) - l_{dq} \cos(2\Delta\theta) \right] \tag{7}
$$

or, equivalently:

$$
I_{hq} = -\frac{I_h}{2} \sqrt{l_\Delta^2 + l_{dq}^2} \sin(2\Delta\theta - 2\varepsilon) \tag{8}
$$

The signal I_{hq} is related to the convergence region of the sensorless drive since it is the signal that the position observer (a PI+I) tries to nullify in order to find the stable convergence points [13].

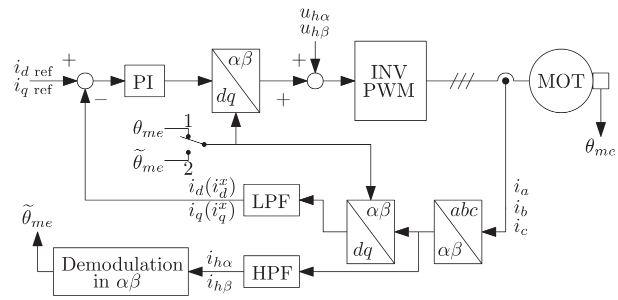

Fig. 6. Control scheme for anisotropic synchronous machines drives: rotating injection in $\alpha\beta$ and demodulation. When the switch is on position 1, the control operates on the measured dq reference frame (sensored operation). When the switch is on position 2, the control operates on the estimated $d^x q^x$ reference frame (sensorless operation).

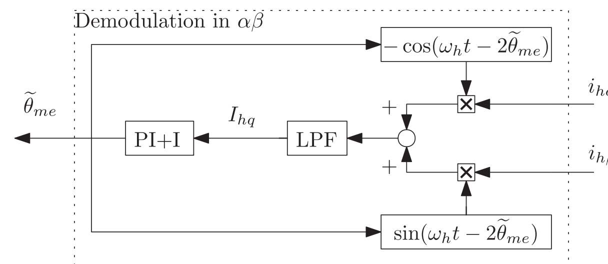

Fig. 7. Demodulation scheme in $\alpha\beta$.

B. Sinusoidal Injection in $\alpha\beta$ (rotating)

Sensorless control schemes for rotor position estimation at standstill or low speed can operate with a pulsating injection on d^x but also with of a rotating injection in α-β. The scheme is shown in Fig. 6. A sinusoidal rotating injection in α-β:

$$
\begin{aligned}
u_{h\alpha} &= U_h \cos(\omega_h t) \\
u_{h\beta} &= U_h \sin(\omega_h t)
\end{aligned} \tag{9}
$$

leads to high frequency currents:

$$
\begin{aligned}
i_{h\alpha} &= I_h \left[l_\Sigma \sin(\omega_h t) + \sqrt{l_\Delta^2 + l_{dq}^2} \sin(\omega_h t - 2\widetilde{\theta}_{me}) \right] \\
i_{h\beta} &= I_h \left[-l_\Sigma \cos(\omega_h t) + \sqrt{l_\Delta^2 + l_{dq}^2} \cos(\omega_h t - 2\widetilde{\theta}_{me}) \right]
\end{aligned} \tag{10}
$$

The hf currents $i_{h\alpha}$ and $i_{h\beta}$ contain information on the rotor position $\widetilde{\theta}_{me}$. Heterodyning demodulation, shown in Fig. 7, is the conventional approach to retrieve the rotor position estimation: $i_{h\alpha}$ is multiplied for $-\cos(\omega_h t - 2\widetilde{\theta}_{me})$, $i_{h\beta}$ for $\sin(\omega_h t - 2\widetilde{\theta}_{me})$. The results of the products are summed and filtered with a LPF. The result of the demodulation (input of the position observer) is the signal:

$$
I_{hq} = -I_h \sqrt{l_\Delta^2 + l_{dq}^2} \sin(2\Delta\theta - 2\varepsilon) \tag{11}
$$

The signal I_{hq} in the case of rotating injection in $\alpha\beta$ (11) is equal to the one in the case of pulsating injection (8) apart from a factor 2 in the denominator. Therefore, the convergence region

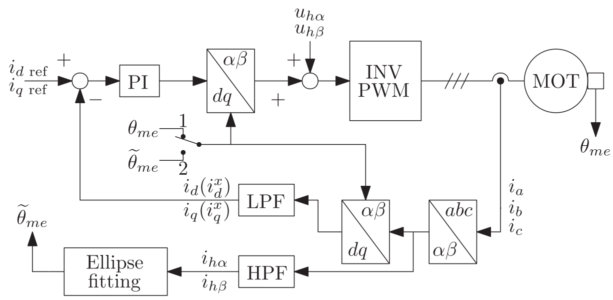

Fig. 8. Control scheme with rotating injection in $\alpha\beta$ and ellipse fitting. When the switch is on position 1, the control operates on the measured dq reference frame (sensored operation). When the switch is on position 2, the control operates on the estimated $d^x q^x$ reference frame (sensorless operation).

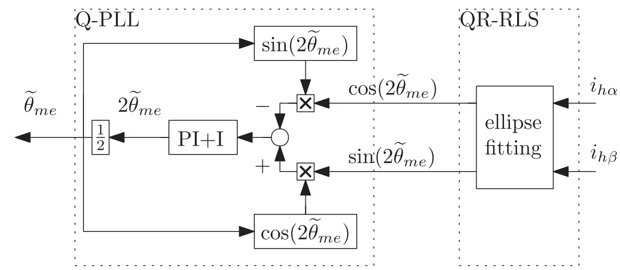

Fig. 9. Detail of the ellipse fitting for rotating injection in $\alpha\beta$, consisting of the QR-RLS (the ellipse fitting itself) and the Q-PLL.

will be the same, being this region a property of the motor itself and not depending on the considered injection technique.

C. Ellipse Fitting

When a rotating injection in the $\alpha\beta$ reference frame is adopted, besides the heterodyning demodulation described in the previous sub-section, also an ellipse fitting technique can be adopted to estimate the rotor position. In comparison with the demodulation, the ellipse fitting approach has a reduced number of filters and tunable parameters. It is based on the consideration that the hf current in the α-β reference frame traces an ellipse whose orientation is related to the rotor position. A buffer of current samples is considered and elaborated adopting a Recursive Least Squares (QR-RLS) ellipse fitting combined with an orthogonal PLL (Q-PLL). The ellipse fitting scheme is shown in detail in Fig. 8. Major details and a full development of the adopted ellipse fitting technique can be found in [17], [18].

III. FEA Computation of the Convergence Region

The conventional procedure to predict the self-sensing capabilities of a synchronous sensorless drive consists in processing the flux linkage maps. In this section the procedure to compute the convergence region starting from FEA computations is described. A detailed and systematic description of the adopted approach can be found in [13]. The self-sensing capabilities, i.e. the hf saliency, the open-loop estimation error and the convergence region, explain and predict the performance of a sensorless drive in the case of signal injection methods. Given a reference trajectory for the current control (usually the MTPA), the trajectories t_1 and t_2 can be computed. The sensored trajectory t_1 is the trajectory of the position observer in open loop during a sensored operation, while the sensorless trajectory t_2 is the trajectory of the effective operating points controlling the motor in sensorless operation. It is worth noticing that trajectory t_1 is fictitious and it is not covered either during sensored control or during sensorless control. Fig. 10 shows the convergence regions of the PMA-SynRM and the SynRM computed on the simulated flux linkages maps. The MTPA is set as current reference. The sensored trajectory t_1 moves away from the MTPA reference for increasing current values because of the cross-saturation effect

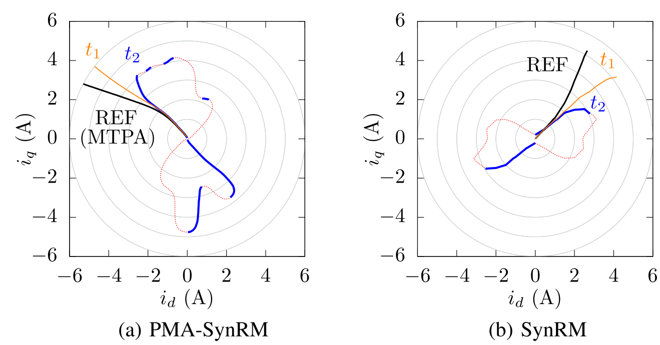

Fig. 10. Convergence region computed from the simulated flux linkages maps (FEA) for $\theta_{me} = 0$, using the method presented in [13]. The MTPA trajectory is used as reference for the current loop. t_1 is the sensored trajectory, t_2 the sensorless trajectory.

on the estimated rotor position [10]. The difference between the estimated position $\widetilde{\theta}_{me}$ and the rotor (measured) position θ_{me} is the open-loop estimation error ε defined as [13]:

$$\begin{aligned} \varepsilon &= \frac{1}{2}\,\mathrm{atan2}(-l_{dq}, l_{\Delta}) && \text{PMS-SynRM} \\ \varepsilon &= \frac{1}{2}\,\mathrm{atan2}(l_{dq}, -l_{\Delta}) && \text{SynRM} \end{aligned} \tag{12}$$

As can be noticed, the sensorless trajectory t_2 has a shorter length than t_1 because it exists a working point beyond which the observer is not able to estimate the rotor position leading to the sensorless control divergence [12]. The maximum length of trajectory t_2 is about 4 A in the case of PMA-SynRM, meaning that the motor can operate in sensorless operation up to this current amplitude (without adopting compensations). The maximum length of t_2 for the SynRM is about 3 A. For higher current values it is not possible to estimate the rotor position, and additional compensations should be adopted [11], [12], [19]. It is worth noticing that the analysis and test considered in this paper are carried out all at locked rotor, i.e. for a fixed $\theta_{me} = 0$. Due to the possible variation of the flux-linkage characteristics with the rotor position, a change in such a trajectory may exist.

The open source project dolomites-apollo has been adopted for the computation of the convergence region [15].

(a) Locked PMA-SynRM

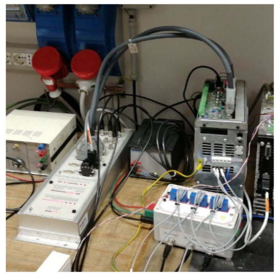

(b) dSPACE1104 and inverter

Fig. 11. Experimental setup.

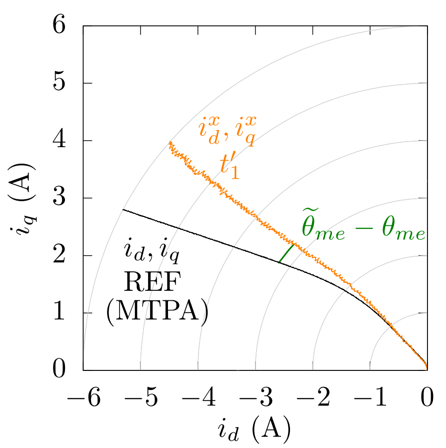

Fig. 12. PMA-SynRM: measured trajectory t_1'. The currents i_d, i_q and the estimated position in open-loop $\widetilde{\theta}_{me}$ are used to compute the currents i_d^x, i_q^x. Rotor locked at $\theta_{me} = 0$. Adopted rotor position estimation technique: ellipse fitting.

IV. Experimental Measurement of the Convergence Region

In Section III the sensored trajectory t_1 and the sensorless trajectory t_2 have been computed through post-processing computations on the FEA maps. In the following, the trajectories t_1' and t_2' will be recorded online during two experimental tests (the first sensored and the second sensorless) using the MTPA as reference trajectory for the current control. The tests have been performed on the test bench shown in Fig. 11, where the motors have been locked at $\theta_{me} = 0$. The control scheme has been implemented on a dSPACE1104 using a control frequency of 10 kHz. The amplitude of the voltage injection is $U_h = 40$ V, and the injection frequency is $f_h = 1$ kHz.

It is worth noticing the presence of the encoder in the control scheme in Figs. 6 and 8. The measured position θ_{me} can be used for the sensored operation (switch on position 1) to measure trajectory t_1' but also during the sensorless operation (switch on position 2) to identify the sensorless trajectory t_2', which is one of the goals of the paper. The control scheme reported in Fig. 4 is not suitable to measure the trajectory t_1' adopting the pulsating injection. It should be modified considering different dq transformations for the current loop and for the high frequency injection. For this reason the rotating injection is mainly

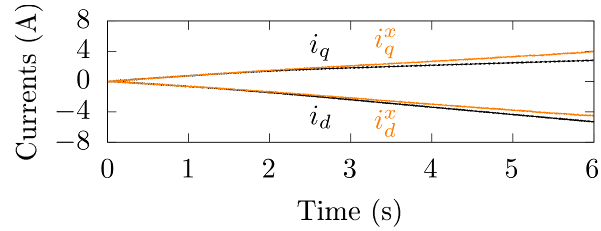

(a) Stator currents measured in the actual dq rotor reference frame. Stator currents computed in the shifted $d^x q^x$ reference frame

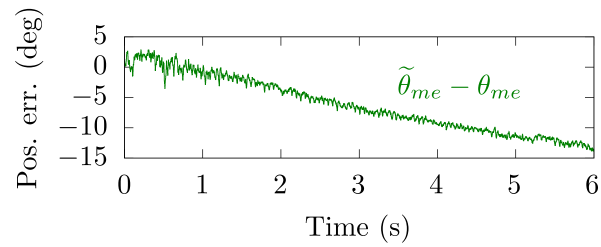

(b) Difference between estimated and measured rotor position

Fig. 13. PMA-SynRM: details of quantities during the measure of trajectory t_1' of Fig. 12.

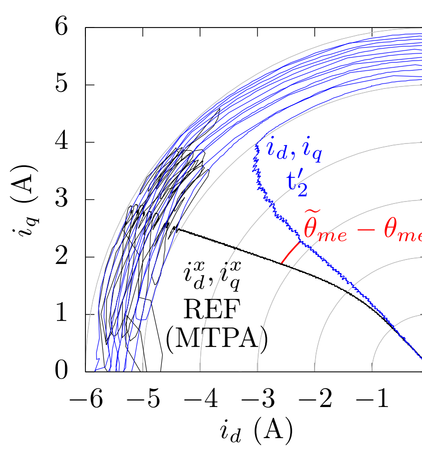

Fig. 14. PMA-SynRM: mesured trajectory t_2'. The currents i_d^x, i_q^x and the estimated position in closed-loop $\widetilde{\theta}_{me}$ are used to compute the currents i_d, i_q. Rotor locked at $\theta_{me} = 0$. Adopted rotor position estimation technique: ellipse fitting.

considered in the paper investigating the measurement of the sensorless trajectories with two different demodulation techniques (demodulation and ellipse fitting). Nevertheless, results with the pulsating injection are considered when possible for a further comparisons, in particular for the t_2' trajectory.

The first test is performed in sensored mode: the measured position $\theta_{me} = 0$ is used for the current control (the switch in Figs. 6 and 8 is on position 1) while the estimated position $\widetilde{\theta}_{me}$ and the currents i_d and i_q are used for the online computation of the trajectory t_1'.

The coordinates of trajectory t_1', i.e. the currents in the estimated $d^x q^x$ reference frame i_d^x and i_q^x, are computed as:

$$\begin{aligned} i_d^x &= i_d \cos(\widetilde{\theta}_{me} - \theta_{me}) - i_q \sin(\widetilde{\theta}_{me} - \theta_{me}) \\ i_q^x &= i_d \sin(\widetilde{\theta}_{me} - \theta_{me}) + i_q \cos(\widetilde{\theta}_{me} - \theta_{me}) \end{aligned} \tag{13}$$

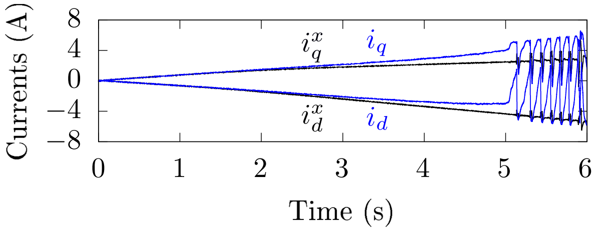

(a) Stator currents measured in the shifted $d^x q^x$ reference frame. Stator currents computed in the actual dq reference frame

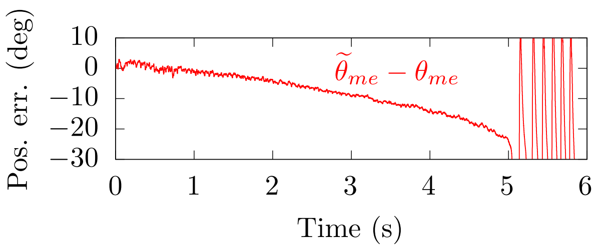

(b) Difference between estimated and measured rotor position

Fig. 15. PMA-SynRM: details of quantities during the measure of trajectory t_2' of Fig. 14.

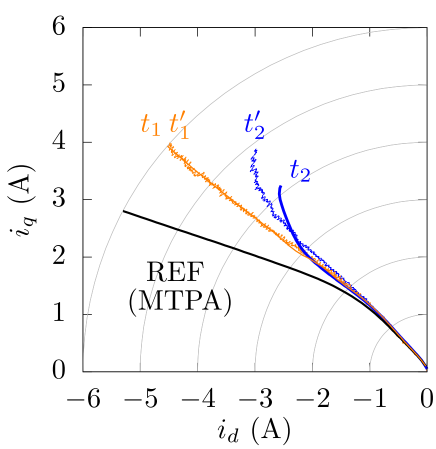

Fig. 16. PMA-SynRM: comparison between simulated and measured sensorless trajectories. Adopted rotor position estimation technique: ellipse fitting.

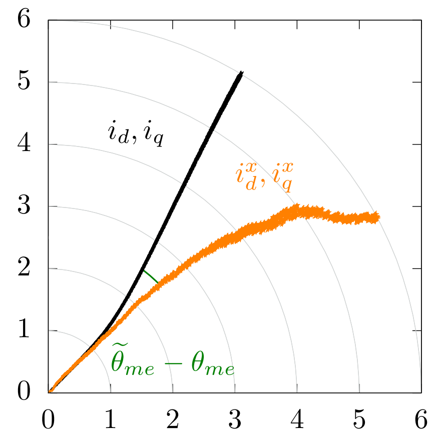

Fig. 17. SynRM: measured trajectory t_1'. The currents i_d, i_q and the estimated position in open-loop $\widetilde{\theta}_{me}$ are used to compute the currents i_d^x, i_q^x. Rotor locked at $\theta_{me} = 0$. Adopted rotor position estimation technique: ellipse fitting.

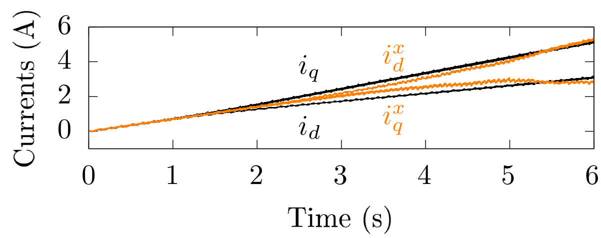

(a) Stator currents measured in the actual dq rotor reference frame. Stator currents computed in the shifted $d^x q^x$ reference frame

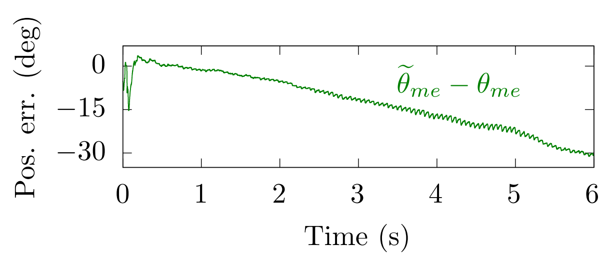

(b) Difference between estimated and measured rotor position

Fig. 18. SynRM: details of quantities during the measure of trajectory t_1' of Fig. 17.

It is worth noticing that in this test the difference between the estimated position $\widetilde{\theta}_{me}$ and the measured position θ_{me} is the open-loop estimation error ε.

The second test is performed in sensorless mode: the estimated position $\widetilde{\theta}_{me}$ is used for the current control (the switch in Figs. 6 and 8 is in position 2) while the measured position $\theta_{me} = 0$ and the currents i_d^x and i_q^x are used for the online computation of the trajectory t_2'. The coordinates of trajectory t_2', i.e. the currents in the actual dq reference frame i_d and i_q, are computed as:

$$i_d = i_d^x \cos(\widetilde{\theta}_{me} - \theta_{me}) - i_q^x \sin(\widetilde{\theta}_{me} - \theta_{me})$$
$$i_q = i_d^x \sin(\widetilde{\theta}_{me} - \theta_{me}) + i_q^x \cos(\widetilde{\theta}_{me} - \theta_{me}) \quad (14)$$

In the following the obtained results for the two considered motors are described.

A. Pma-Synrm

Fig. 12 shows the measured t_1' trajectory for the PMA-SynRM. The trajectory t_1', which coordinates are the currents i_d^x and i_q^x, is rotated with respect to the reference trajectory of a growing angle equal to ε. The time behavior of the current and other relevant quantities during the test are shown in Fig 13. The tests are performed imposing a ramp of commanded current along the MTPA. The amplitude of the current reference grows at rate of 1 A per second. Fig. 13 a shows the measured currents i_d and i_q and the computed currents i_d^x and i_q^x. The actual operating points (i_d, i_q) follow the trajectory MTPA from (0,0) up to the rated current amplitude value (6 A). The currents i_d^x and i_q^x represent the coordinates of trajectory t_1'. Fig. 13 b shows the estimation error, which is

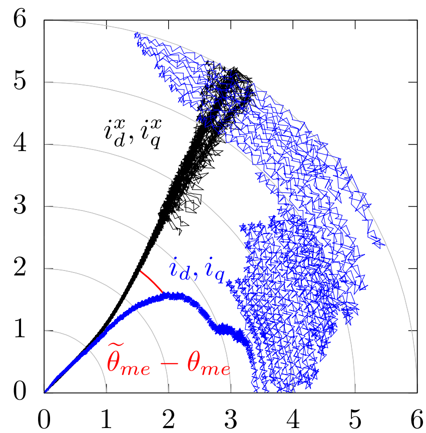

Fig. 19. SynRM: mesured trajectory t_2'. The currents i_d^x, i_q^x and the estimated position in closed-loop $\widetilde{\theta}_{me}$ are used to compute the currents i_d, i_q. Rotor locked at $\theta_{me} = 0$. Adopted rotor position estimation technique: ellipse fitting.

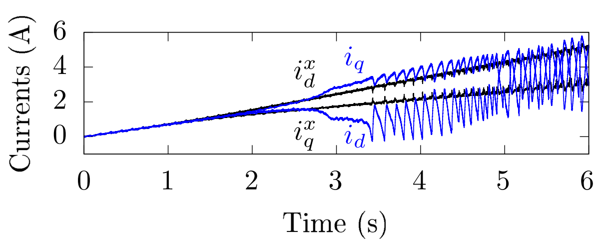

(a) Stator currents measured in the shifted $d^x q^x$ reference frame. Stator currents computed in the actual dq reference frame

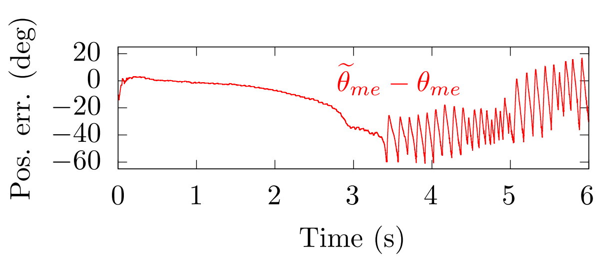

(b) Difference between estimated and measured rotor position

Fig. 20. SynRM: details of quantities during the measure of trajectory t_2' of Fig. 19.

null at zero currents and increases up to -15 electrical degrees at the rated current amplitude. The results of the second test are shown both on the dq plane, Fig. 14, and as a function of time, Fig. 15. The motor is operated in sensorless control using a reference current ramp along the MTPA. The operating reference frame is the estimated $d^x q^x$ since the current control is closed on the estimated position $\widetilde{\theta}_{me}$. The measured currents i_d^x and i_q^x appear to follow the MTPA reference in the shifted control frame, but the real operating point is in a different place (t_2'). The actual operating point i_d-i_q is different from the trajectory covered in the first test (i.e. the MTPA), thus during a sensorless test - in which no compensations are actuated - the motor is actually controlled along a wrong load-dependent current reference. Since the motor parameters are not linear and depend on the operating point, the trajectory t_2' crosses a region of the dq plane where the inductances l_{dq} and l_Δ are different from those encountered along the MTPA trajectory. As a consequence, the closed-loop estimation error in Fig. 15 a is different from the open-loop estimation error in Fig. 13 b. While the open-loop estimation ε error has a direct expression, i.e. (12), the closed-loop estimation error requires some additional steps to be computed. In particular, the sensorless trajectory t_2 can be computed from the signal I_{hq}, defined in (11) [13]. As concerns the trajectory t_2' recorded during the second test, it is possible to notice that it is more distant from the MTPA than the sensored trajectory t_1'. Moreover, at a current amplitude of 5 A (at time 5 s) the control diverges. This can be noted also in the oscillations of i_d^x, i_q^x, i_d and i_q (in Fig. 15 a) and of $\widetilde{\theta}_{me}$ (in Fig. 15 b). The phenomenon of sensorless control divergence happens in the regions of the dq plane where the signal I_{hq} does not cross the zero for any current angle [12]. When the position estimation and the control are lost, the sensorless drive becomes unusable.

To conclude, the trajectories computed during the experimental tests are compared and validated with the trajectories obtained from the FEA flux-linkages maps in Fig. 16. The comparison is done considering t_1 and t_2 (from Fig. 10), t_1' (from Fig. 12), and t_2' (from Fig. 14). In Fig. 16 it is possible to appreciate that standstill operation and quasi-steady-state current control make the experimental results - t_1' and t_2' - comparable with the prediction assuming an ideal control - t_1 and t_2. In particular, the sensored trajectories t_1 and t_1' are in very good agreement. Regarding the sensorless trajectories, the FEA trajectory t_2 is truncated at a current amplitude of 4 A while the experimental trajectory t_2' reaches the current amplitude of 5 A. The control diverges for a current amplitude inferior to the rated value in both cases, indicating that the adopted motor is not completely suitable for signal injection sensorless control.

B. Synrm

The same experimental tests have been repeated considering the SynRM motor of Figs. 1 b. 17 shows the measured t_1' trajectory and Fig. 18 shows a detail of the main quantities during the test. As for the results described in Section IV-A the ellipse fitting technique has been adopted for the rotor position estimation. In particular, also in this case it can be noted that the position estimation error increases with the current amplitude, see Fig. 18 b.

The results obtained for the measure of the trajectory t_2' are shown in Fig. 19. Fig. 20 shows the details of the main quantities during the test. Also in this case the current trajectory in the estimated reference frame $d^x q^x$ appears along the MTPA trajectory. The deviation of the t_2' trajectory from the MTPA is clearly visible as well as the divergence of the estimator for a current amplitude of about 3.5 A at 3.5 s.

Finally, Fig. 21 shows the comparison between simulated and measured trajectories. Trajectories t_1 and t_2 are the same as in Fig. 10. t_1' and t_2' are as in Figs. 17 and 19 respectively. Also in this case a satisfactory agreement can be observed between predicted and measured trajectories.

C. Measurements of Trajectories Considering Different Demodulating Techniques

The results so far presented consider the control scheme reported in Fig. 8 adopting a rotating injection in $\alpha\beta$ with the

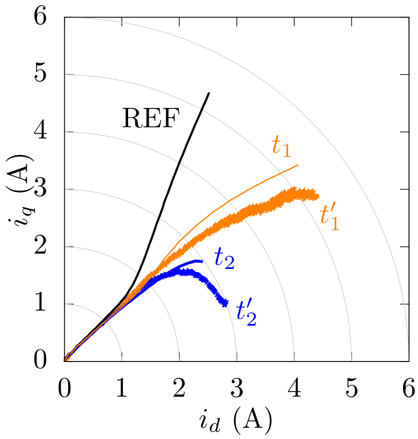

Fig. 21. SynRM: comparison between simulated and measured sensorless trajectories. Adopted rotor position estimation technique: ellipse fitting.

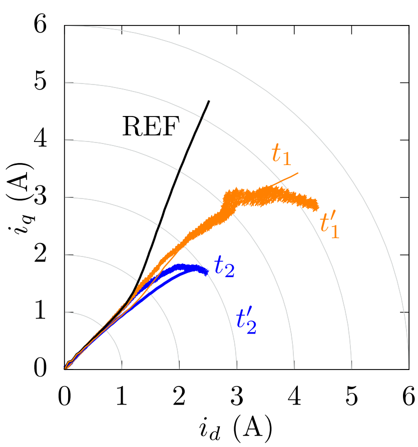

Fig. 22. SynRM: comparison between simulated and measured sensorless trajectories. Adopted rotor position estimation technique: rotating injection and demodulation.

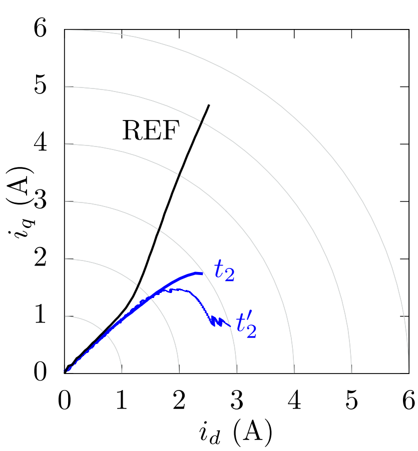

Fig. 23. SynRM: comparison between simulated and measured sensorless trajectories. Adopted rotor position estimation technique: pulsating injection and demodulation.

ellipse fitting technique. Nevertheless, similar results can be achieved considering also different injection and demodulation techniques. This section describes in particular the measurements of the sensorless control trajectories on the SynRM motor which have been carried out adopting also demodulation techniques considering both rotating and pulsating injections.

Fig. 22 shows the simulated and measured trajectories when rotating injection and the classical demodulation scheme of Fig. 7 is adopted. Since the injection is performed in the $\alpha\beta$ stationary reference frame both t_1' and t_2' can be measured.

Fig. 23 shows the measured t_2' trajectory when pulsating injection is considered adopting the demodulation scheme of Fig. 5. In this case, t_1 trajectory cannot be measured since the entire control works in the estimated $d^x q^x$ reference frame.

It can be noted that the measured trajectories are slightly different considering the various injection and demodulation techniques. Nevertheless, all the measured trajectories are in satisfactory agreement with the simulations.

V. Conclusion

In this article, an experimental investigation about the convergence region of a sensorless drive has been presented and adopted. The self-sensing capability of the drive has been described and highlighted by the difference between the sensored and the sensorless operation trajectories, t_1 and t_2 respectively. Both the trajectories can be evaluated online with proper measurements adopting a standard drive equipped with a position sensor.

In the article, simulations and experimental results are compared. In particular, different injection and demodulation techniques have been considered in the paper. It has been shown that the results obtained considering different control strategies are in satisfactory agreement, also considering simulation results.

References

[1] J. Kim, I. Jeong, K. Nam, J. Yang, and T. Hwang, "Sensorless control of PMSM in a ultra high speed region taking iron loss into account," in *Proc. IEEE Energy Convers. Congr. Expo.*, 2014, pp. 2469–2476, doi: 10.1109/ECCE.2014.6953569.

[2] J. Yoo, H.-S. Kim, and S.-K. Sul, "Design of frequency-adaptive flux observer in PMSM drives robust to discretization error," *IEEE Trans. Ind. Electron.*, vol. 69, no. 4, pp. 3334–3344, Apr. 2022, doi: 10.1109/TIE.2021.3075854.

[3] P. Niedermayr, L. Alberti, S. Bolognani, and R. Abl, "Implementation and experimental validation of ultra high-speed PMSM sensorless control by means of extended Kalman filter," *IEEE J. Emerg. Sel. Topics Power Electron.*, vol. 10, no. 3, pp. 3337–3344, Jun. 2022, doi: 10.1109/JESTPE.2020.3041026.

[4] R. D. Lorenz, "Practical issues and research opportunities when implementing zero speed sensorless control," in *Proc. IEEE 5th Int. Conf. Elect. Mach. Syst.*, 2001, pp. 1–10.

[5] Y.-s. Jeong, R. D. Lorenz, T. M. Jahns, and S. K. Sul, "Initial rotor position estimation of an interior permanent-magnet synchronous machine using carrier-frequency injection methods," *IEEE Trans. Ind. Appl.*, vol. 41, no. 1, pp. 38–45, Jan./Feb. 2005, doi: 10.1109/TIA.2004.840978.

[6] S.-K. S. Sul and S. Kim, "Sensorless control of IPMSM: Past, present, and future," *IEEJ J. Ind. Appl.*, vol. 1, no. 1, pp. 15–23, 2012.

[7] W. Hammel and R. M. Kennel, "Position sensorless control of PMSM by synchronous injection and demodulation of alternating carrier voltage," in *Proc. IEEE 1st Symp. Sensorless Control Elect. Drives*, 2010, pp. 56–63.

[8] S. Kim, J.-I. Ha, and S. K. Sul, "PWM switching frequency signal injection sensorless method in IPMSM," *IEEE Trans. Ind. Appl.*, vol. 48, no. 5, pp. 1576–1587, Sep./Oct. 2012, doi: 10.1109/TIA.2012.2210175.

[9] G. Wang, D. Xiao, G. Zhang, C. Li, X. Zhang, and D. Xu, "Sensorless control scheme of IPMSMs using HF orthogonal square-wave voltage injection into a stationary reference frame," *IEEE Trans. Power Electron.*, vol. 34, no. 3, pp. 2573–2584, Mar. 2019, doi: 10.1109/TPEL.2018.2844347.

[10] P. Guglielmi, M. Pastorelli, and A. Vagati, "Cross-saturation effects in IPM motors and related impact on sensorless control," *IEEE Trans. Ind. Appl.*, vol. 42, no. 6, pp. 1516–1522, Nov./Dec. 2006, doi: 10.1109/TIA.2006.882646.

[11] Y. C. Kwon, J. Lee, and S. K. Sul, "Extending operational limit of IPMSM in signal-injection sensorless control by manipulation of convergence point," *IEEE Trans. Ind. Appl.*, vol. 55, no. 2, pp. 1574–1586, Mar./Apr. 2019, doi: 10.1109/TIA.2018.2882483.

[12] V. Manzolini and S. Bolognani, "On the rotor position self-sensing capability of reluctance and IPM synchronous motors," *IEEE Trans. Ind. Appl.*, vol. 56, no. 4, pp. 3755–3766, Jul./Aug. 2020, doi: 10.1109/TIA.2020.2984406.

[13] M. Berto, L. Alberti, V. Manzolini, and S. Bolognani, "Computation of self-sensing capabilities of synchronous machines for rotating high frequency voltage injection sensorless control," *IEEE Trans. Ind. Electron.*, vol. 69, no. 4, pp. 3324–3333, Apr. 2022, doi: 10.1109/TIE.2021.3071710.

[14] M. Berto, L. Alberti, and S. Bolognani, "Experimental investigation on the self-sensing capability of synchronous machines for signal injection sensorless drives," in *Proc. IEEE Energy Convers. Congr. Expo.*, 2021, pp. 5078–5083, doi: 10.1109/ECCE47101.2021.9595287.

[15] [Online]. Available: https://gitlab.com/LuigiAlberti/dolomites-python

[16] L. Alberti, N. Bianchi, and S. Bolognani, "High-frequency d–q model of synchronous machines for sensorless control," *IEEE Trans. Ind. Appl.*, vol. 51, no. 5, pp. 3923–3931, Sep./Oct. 2015, doi: 10.1109/TIA.2015.2428222.

[17] F. Toso, M. Berto, L. Alberti, and F. Marcuzzi, "Efficient QR updating factorization for sensorless synchronous motor drive based on high frequency voltage injection," *IEEE Trans. Ind. Electron.*, vol. 67, no. 12, pp. 10213–10222, Dec. 2020, doi: 10.1109/TIE.2019.2959478.

[18] L. Ortombina, M. Berto, and L. Alberti, "Sensorless drive for salient synchronous motors based on direct fitting of elliptical-shape high-frequency currents," *IEEE Trans. Ind. Electron.*, vol. 70, no. 4, pp. 3394–3403, Apr. 2023, doi: 10.1109/TIE.2022.3177753.

[19] B. Shuang, Z. Q. Zhu, and X. Wu, "Improved cross-coupling effect compensation method for sensorless control of IPMSM with high frequency voltage injection," *IEEE Trans. Energy Convers.*, vol. 37, no. 1, pp. 347–358, Mar. 2022, doi: 10.1109/TEC.2021.3093361.

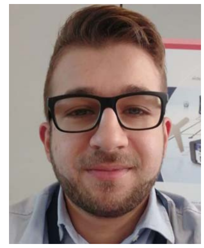

Matteo Berto was born in Venice, Italy. He received the B.S. and M.S. degrees in electrical engineering in 2016 and 2018, respectively, from the University of Padova, Padova, Italy, where he is currently working toward the Ph.D. degree with the Electrical Drives Laboratory. His main research focuses on sensorless control for AC motors.

Luigi Alberti (Senior Member, IEEE) received the Laurea and the Ph.D. degrees in electrical engineering from the University of Padova, Padova, Italy, in 2005 and 2009, respectively. From 2009 to 2012, he was a Research Associate with the University of Padova. In 2012, he moved to the Faculty of Science and Technology, Free University of Bozen-Bolzano, Bolzano, Italy, to start research and educational activities in the field of electrical engineering and electrical machines. He is currently an Associate Professor with the Department of Industrial Engineering, University of Padova, working on design, analysis, and control of electric machines and drives, with particular interest in renewable energies and more electric vehicles.

Silverio Bolognani (Fellow, IEEE) received the Laurea degree in electrical engineering from the University of Padova, Padova, Italy, in 1976. He is the author of three patents and more than 250 international publications. He was the Head of the Department of Electrical Engineering from 2001 to 2008, a Member of the Scientific Committee from 2004 to 2008, the Vice-Rector for the Research from 2009 to 2015 with the same University. He is currently a Full Professor of electrical converters, machines and drives with the University of Padova. He is the Chairman of the IEEE IAS/IES/PELS North Italy Joint Chapter, a Member of the Scientific Committee of national and international conferences and associations.

Open Access funding provided by 'Università degli Studi di Padova' within the CRUI CARE Agreement